



Influence of Operation Parameters on Thermohydraulic Performance of Supercritical CO₂ in a Printed Circuit Heat Exchanger

Lei Chai & Savvas A. Tassou

To cite this article: Lei Chai & Savvas A. Tassou (01 Aug 2024): Influence of Operation Parameters on Thermohydraulic Performance of Supercritical CO₂ in a Printed Circuit Heat Exchanger, Heat Transfer Engineering, DOI: [10.1080/01457632.2024.2384157](https://doi.org/10.1080/01457632.2024.2384157)

To link to this article: <https://doi.org/10.1080/01457632.2024.2384157>



© 2024 The Author(s). Published with license by Taylor & Francis Group, LLC



Published online: 01 Aug 2024.



Submit your article to this journal [↗](#)



Article views: 86



View related articles [↗](#)



View Crossmark data [↗](#)

Influence of Operation Parameters on Thermohydraulic Performance of Supercritical CO₂ in a Printed Circuit Heat Exchanger

Lei Chai  and Savvas A. Tassou

Centre for Sustainable Energy Use in Food Chain (CSEF), Institute of Energy Futures, Brunel University London, Uxbridge, Middlesex, UK

ABSTRACT



The performance of recuperative printed circuit heat exchangers is critical in supercritical CO₂ (sCO₂) power generation applications. This article presents a three-dimensional numerical model of sCO₂ flowing in a printed circuit heat exchanger and investigates its thermohydraulic performance under different operation conditions. The simulations employ the standard $k-\varepsilon$ turbulent model, and consider entrance effects, conjugate heat transfer, real gas thermophysical properties and buoyancy effects. The heat exchanger operation parameters cover mass flux from 254.6 to 1273.2 kg/m²s, inlet temperature 50–150 °C and outlet pressure 100–250 bar on the cold side, and 300–500 °C and 75–150 bar on the hot side. Results show that increasing CO₂ mass flux leads to a significantly increased heat transfer coefficient, a slight increase in temperature difference between the hot and cold CO₂, as well as larger pressure drop and lower friction factor on both sides. Increasing the cold CO₂ pressure, decreasing the cold CO₂ temperature, and increasing the hot CO₂ temperature result in a higher heat transfer rate of the heat exchanger. Increasing the CO₂ temperature on each side causes increased pressure drops on both sides. Increasing the CO₂ pressure on each side reduces the pressure drop on each side.

Introduction

Due to its attractive thermophysical properties, CO₂ has many advantages over other competing high-temperature heat to power conversion technologies [1, 2]. Numerous studies have shown that the sCO₂ (supercritical CO₂) Brayton cycle has the potential for smaller equipment sizes, smaller plant footprint, better operational flexibility, and higher cycle efficiency [3]. A contributing factor to the high efficiency is the high degree of thermal recuperation that can be achieved between the expander exhaust and the compressor exhaust. An important challenge in maximizing this recuperation is to select a recuperative heat exchanger that has high heat transfer effectiveness, relatively low pressure drop in both the hot and cold flow streams and can withstand high temperatures and pressures and thermal shocks [4]. Amongst the various types of recuperative heat exchangers, the printed circuit heat exchanger (PCHE) has become a preferred choice due to its highly compact construction, high heat transfer coefficients, and capability to operate effectively over

high-pressure differentials and wide range of operating temperatures [5].

A printed circuit heat exchanger is a compact heat exchanger with an effective surface area density of up to 2500 m²/m³. Two advanced technologies are utilized to manufacture the PCHE: photo etching and diffusion bonding. Flat metal plates are photo-chemically etched with specific design patterns and joined by a diffusion-bonding process to form a compact, strong, all-metal structure containing complex internal passages that allow for good flow control and fluid metering features [6]. For the sCO₂ Brayton cycle, the PCHE must accommodate a high temperature and significant pressure differentials between the heat exchange fluids and offer excellent thermohydraulic performance. Four main types of PCHE flow passages have been developed, including straight channels, zig-zag (or wavy) channels, channel with S-shaped fins, and channel with aerofoil fins [7]. The development and application of heat transfer theory and knowledge of the behavior of sCO₂ flowing in these channels are

CONTACT Dr. Lei Chai  lei.chai@brunel.ac.uk  Centre for Sustainable Energy Use in Food Chain (CSEF), Institute of Energy Futures, Brunel University London, Uxbridge, Middlesex UB8 3PH, UK.

© 2024 The Author(s). Published with license by Taylor & Francis Group, LLC

This is an Open Access article distributed under the terms of the Creative Commons Attribution License (<http://creativecommons.org/licenses/by/4.0/>), which permits unrestricted use, distribution, and reproduction in any medium, provided the original work is properly cited. The terms on which this article has been published allow the posting of the Accepted Manuscript in a repository by the author(s) or with their consent.

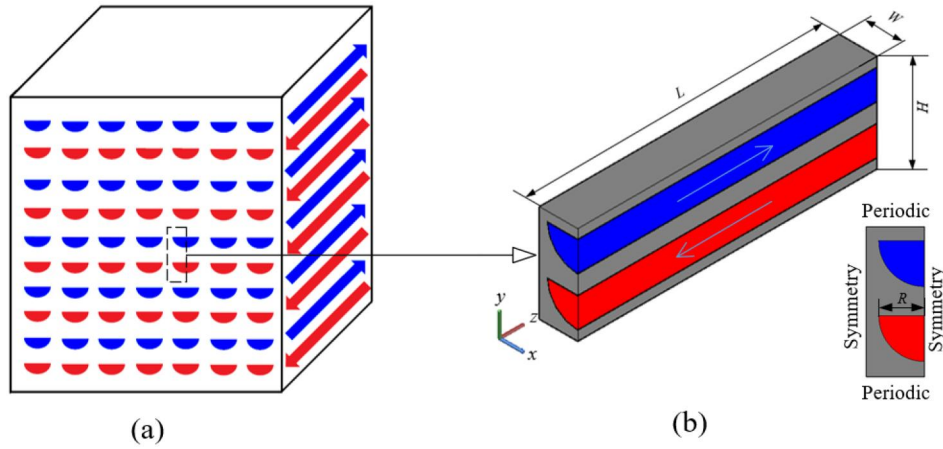


Figure 1. Computational model. (a) Schematic of a printed circuit heat exchanger and (b) Schematic of the computational domain.

assumed to be stacked alternately for the hot and cold fluids. To effectively simulate the sCO₂ flowing in the PCHE, a representative computational domain containing two channels and the surrounding solid is employed in the numerical modeling work as shown in Figure 1b. The cross section of the channels is semi-circular with a radius (R) of 1 mm. The channel pitch is 2.54 mm in the x direction ($2W$) and 3.26 mm in the y direction (H), and the channel length (L) is 272 mm. The cold sCO₂ flows in the upper channel and the hot flows in the lower channel. The parameters of channel geometry are from Refs. [32, 33], in which a printed circuit heat exchanger with straight microchannels was fabricated and tested with helium for high-temperature reactor applications.

Modeling assumptions and conservation equations

The CFD modeling was developed for steady three-dimensional fluid flow and heat transfer. The sCO₂ flow is assumed to be uniformly distributed in the channel inlet with uniform temperature and velocity profiles. Due to the significant variations of thermophysical properties of sCO₂ around the critical point with pressure and temperature, the NIST real gas thermophysical properties are employed in the present work and the buoyancy effects are also considered.

In the fluid domain, the Navier-Stokes equations and the energy equation are simultaneously solved. The continuity, momentum, and energy equations for the sCO₂ flow are as follows:

$$\frac{\partial}{\partial x_i}(\rho u_i) = 0 \quad (1)$$

$$\begin{aligned} \frac{\partial}{\partial x_i}(\rho u_i u_j) = \rho g_j - \frac{\partial p}{\partial x_j} + \frac{\partial}{\partial x_i} \left[\mu \left(\frac{\partial u_j}{\partial x_i} + \frac{\partial u_i}{\partial x_j} \right) \right. \\ \left. + \mu_t \left(\frac{\partial u_j}{\partial x_i} + \frac{\partial u_i}{\partial x_j} \right) - \frac{2}{3} \rho k \delta_{ij} \right] \quad (2) \end{aligned}$$

$$\frac{\partial}{\partial x_i}(\rho u_i c_p T) = \frac{\partial}{\partial x_i} \left(\lambda \frac{\partial T}{\partial x_i} \right) \quad (3)$$

In the solid domain, the Fourier's conduction equation is solved. The heat conduction equation for the solid region is:

$$\frac{\partial}{\partial x_i} \left(\lambda_s \frac{\partial T}{\partial x_i} \right) = 0 \quad (4)$$

where u is the fluid velocity vector, p is the hydrodynamic pressure, ρ , μ , c_p , and λ are the density, dynamic viscosity, specific heat capacity and thermal conductivity of the fluid, respectively. The λ_s is the thermal conductivity of solid material.

For all the tested cases in the present work, the sCO₂ flowing in the channels is fully turbulent with Reynolds numbers in the range 7200 to 76000. The effects of molecular viscosity are negligible, so the standard k - ϵ model is adopted for the turbulent flow simulations.

$$\frac{\partial}{\partial x_i}(\rho k u_i) = \frac{\partial}{\partial x_i} \left[\left(\mu + \frac{\mu_t}{\sigma_k} \right) \frac{\partial k}{\partial x_j} \right] + G_k + G_b - \rho \epsilon \quad (5)$$

$$\begin{aligned} \frac{\partial}{\partial x_i}(\rho \epsilon u_i) = \frac{\partial}{\partial x_i} \left[\left(\mu + \frac{\mu_t}{\sigma_\epsilon} \right) \frac{\partial \epsilon}{\partial x_j} \right] + G_{1\epsilon} \frac{\epsilon}{k} (G_k + G_b) \\ - G_{2\epsilon} \rho \frac{\epsilon^2}{k} \quad (6) \end{aligned}$$

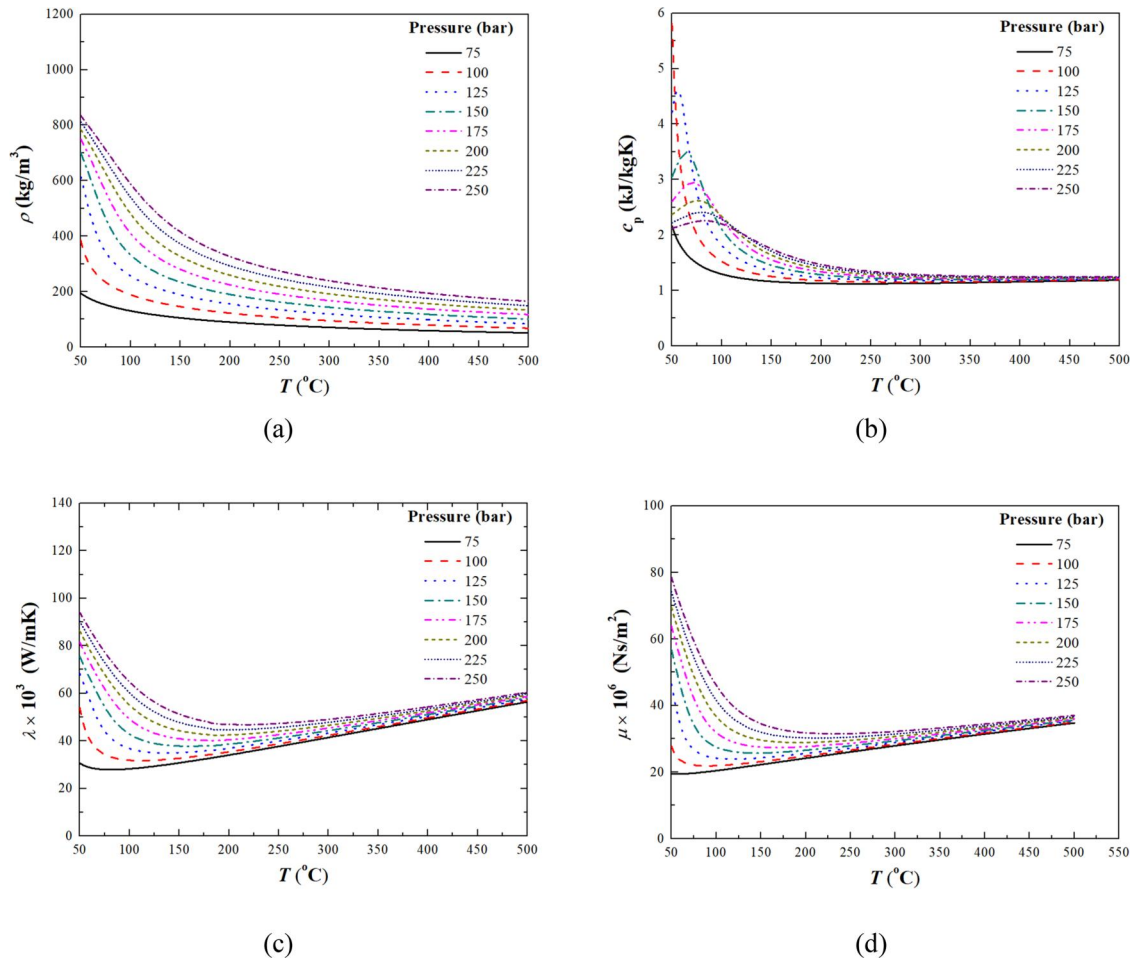


Figure 2. Thermophysical properties of CO₂ at different temperatures and pressures. (a) Density, (b) specific heat, (c) thermal conductivity, and (d) dynamic viscosity.

where μ_t represents the eddy viscosity, G_k represents the generation of turbulence kinetic energy due to the mean velocity gradients and G_b is the generation of turbulence kinetic energy due to buoyancy. The σ_k and σ_ε are the turbulent Prandtl numbers for k and ε , $\sigma_k = 1.0$ and $\sigma_\varepsilon = 1.3$. The $G_{1\varepsilon}$ and $G_{2\varepsilon}$ are constants, $G_{1\varepsilon} = 1.44$ and $G_{2\varepsilon} = 1.92$.

Boundary conditions and solution methods

The numerical simulations were carried out with ANSYS Fluent 2019 R2. Due to the significant variation of thermophysical properties of CO₂ in the near-critical point region, the heat transfer and fluid flow characteristics in the near-critical point region are quite different from those with constant physical properties. Therefore, during the simulations, the NIST real gas models were activated and the REFPROP v9.1 database was dynamically loaded into the solver as a shared library [34]. The material of the surrounding solid was assumed to be stainless steel 316L with thermal conductivity of 16.3 W/(m·K). The

thermophysical properties of sCO₂ at different temperatures and pressures covered by the present study are shown in Figure 2.

For the boundary conditions, the mass-flow-inlet and pressure-outlet boundaries are employed at the inlet ($z=0$ on the cold side and $z=L$ on the hot side) and outlet ($z=L$ on the cold side and $z=0$ on the hot side) of each channel, respectively. At the upper surface ($y=H$) and the lower surface ($y=0$) of the unit cell, the thermally periodic boundary is applied to ensure that the channels thermally interact with virtual adjacent channels. At the left surface ($x=0$) and right surface ($x=W$) of the unit cell, the symmetry boundary is introduced due to the repeated structure. The range of operating conditions for both the hot and cold CO₂ fluids simulated in this study is summarized in Table 1. The operating parameters cover mass flux from 254.6 to 1273.2 kg/(m²·s), inlet temperature 50–150 °C and outlet pressure 100–250 bar on the cold side, and 300–500 °C and 75–150 bar, respectively, on the hot side.

The SIMPLEC algorithm is used to implement the coupling between pressure and velocity, and the second-order upwind is applied to discretize the convection terms in the control volume. The convergence criteria are reached when the normalized residuals of all variables in the momentum and energy equations are less than 10^{-5} . The thickness of the first near-wall mesh was selected to ensure the dimensionless distance from the wall y^+ was in the range from 15 to 50. A grid independence test was also carried out using different mesh sizes. The results in Table 2, show the heat transfer and pressure drop results for the difference mesh sizes for a mass flux of $509.3 \text{ kg}/(\text{m}^2 \cdot \text{s})$, inlet temperature 100°C and outlet pressure 150 bar on the cold side and 400°C and 75 bar on the

Table 1. Range of operating conditions simulated for both the hot and cold fluids.

G ($\text{kg}/\text{m}^2 \cdot \text{s}$)	$p_{\text{cold, out}}$ (bar)	$T_{\text{cold, in}}$ ($^\circ\text{C}$)	$p_{\text{hot, out}}$ (bar)	$T_{\text{hot, in}}$ ($^\circ\text{C}$)
254.6–1273.2	100–250	100	75	400
254.6–1273.2	150	50–150	75	400
254.6–1273.2	150	100	75–150	400
254.6–1273.2	150	100	75	300–500

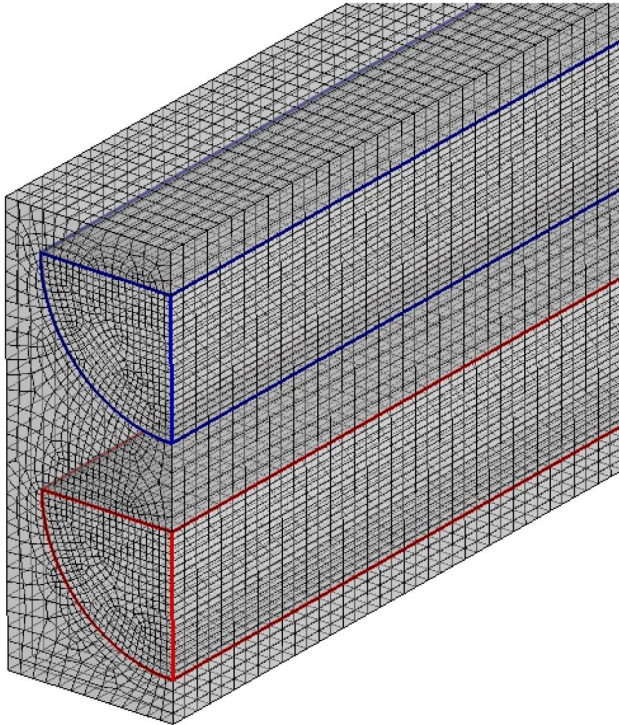


Figure 3. Computational grid for solution domain.

Table 2. Mesh sensitivity with respect to the number of nodes.

Number of nodes	$p_{\text{cold, in}} - p_{\text{cold, out}}$ (kPa)	$p_{\text{hot, in}} - p_{\text{hot, out}}$ (kPa)	\bar{h}_{cold} ($\text{kW}/\text{m}^2 \cdot \text{K}$)	\bar{h}_{hot} ($\text{kW}/\text{m}^2 \cdot \text{K}$)
352,658	3.95	8.18	2.06	2.09
704,898	3.84	8.28	2.03	2.07
1,843,953	3.76	8.34	1.99	2.05
3,686,753	3.75	8.35	1.98	2.04

hot side. Based on the results, a grid size of 1.844 million was chosen for the simulations in the present study. The corresponding mesh configuration is shown in Figure 3.

Data acquisition and model validation

The parameters relevant to thermohydraulic performance include Reynolds number (Re), heat transfer coefficient (h), Nusselt number (Nu), friction factor (f), and heat transfer rate (Q).

The local parameters are defined as

$$Re_z = \frac{GD}{\mu_z} \quad (7)$$

$$h_z = \frac{q_z}{|T_{w,z} - T_{f,z}|} \quad (8)$$

$$Nu_z = \frac{h_z D}{\lambda_{f,z}} \quad (9)$$

$$f_z = \frac{2\rho_z D dp_f}{G^2 dz} \quad (10)$$

where G is the mass flux, D is the hydraulic diameter, q_z , $T_{w,z}$ and $T_{f,z}$ is the local heat flux, local wall temperature, and local fluid temperature at a fixed z plane, respectively. The ρ_z , μ_z and $\lambda_{f,z}$ are the local density, dynamic viscosity, and thermal conductivity of the fluid, respectively. The $\frac{dp_f}{dz}$ represents the pressure gradient just due to the friction, where the pressure gradients caused by the flow acceleration and deceleration due to changes in density were excluded from the total.

The average parameters are defined as

$$\bar{Re} = \frac{\int_0^L Re_z dz}{L} \quad (11)$$

$$\bar{h} = \frac{\int_0^L h_z dz}{L} \quad (12)$$

$$\bar{Nu} = \frac{\int_0^L Nu_z dz}{L} \quad (13)$$

$$\bar{f} = \frac{\int_0^L f_z dz}{L} \quad (14)$$

where L is the channel length.

To validate the numerical model, the numerical results were compared with the predictions of heat transfer and pressure drop from the empirical

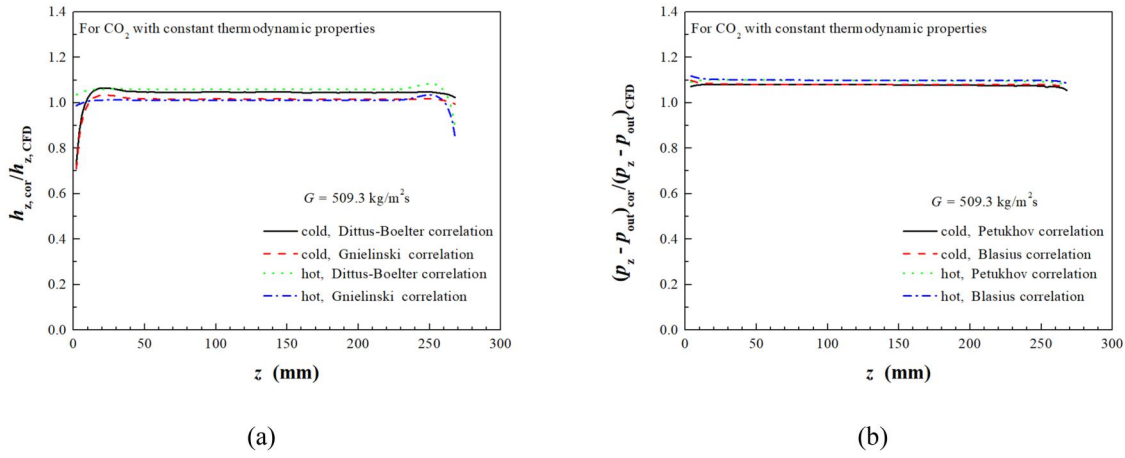


Figure 4. Comparison with predictions from empirical correlations of Dittus-Boelter [35], Gnielinski [36], Blasius [37], and Petukhov [38]. (a) Thermal performance and (b) Hydraulic performance.

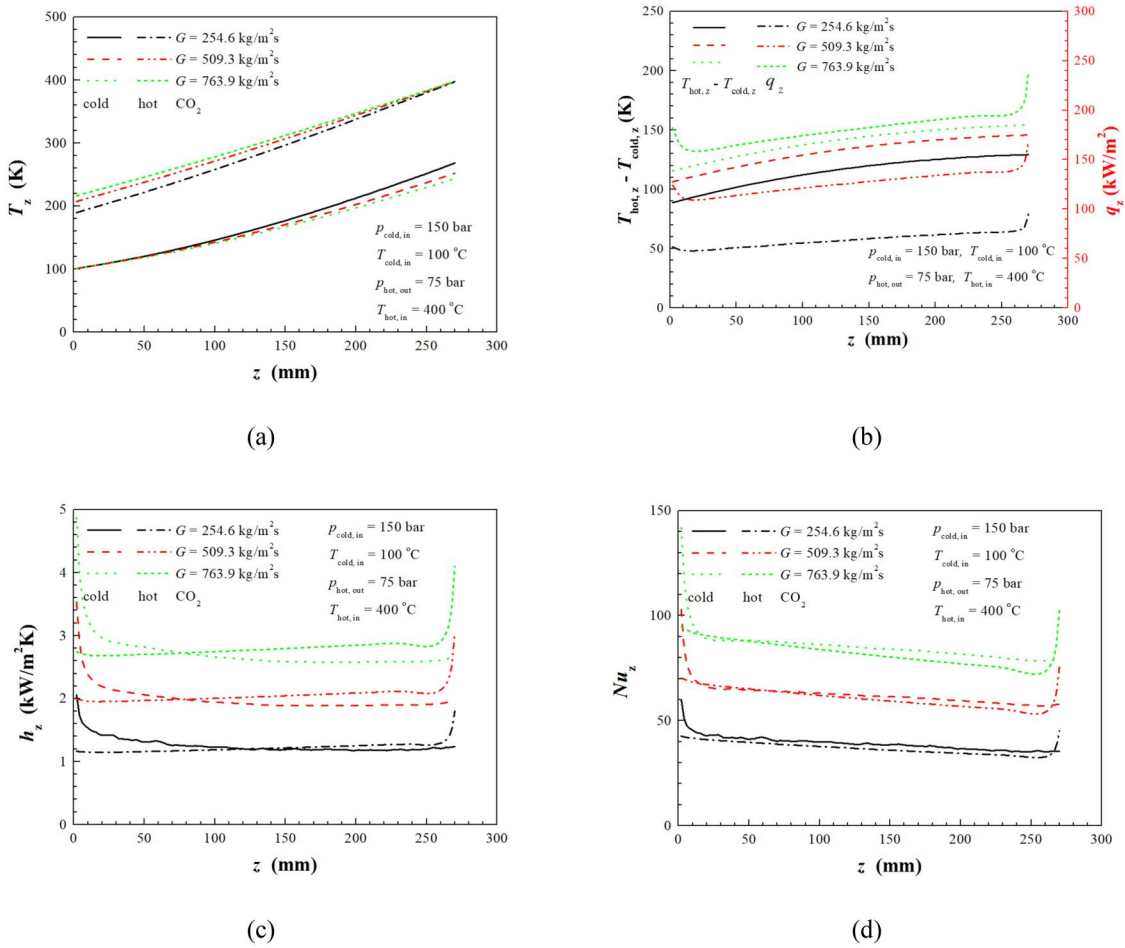


Figure 5. Local thermal performance for different mass fluxes. (a) Fluid temperature, (b) Temperature difference between hot and cold sides and heat flux variation, (c) Heat transfer coefficient, and (d) Nusselt number.

correlations. The Dittus-Boelter correlation [35] is a traditional expression for heat transfer calculations for flows in tubes. The Gnielinski correlation [36] is a more complicated expression that can lead to more accurate results for fully developed turbulent flow in smooth tubes. Figure 4 shows the comparison results

of the case with mass flux of $509.3 \text{ kg/(m}^2 \cdot \text{s)}$, inlet temperature $100 \text{ }^\circ\text{C}$ and outlet pressure 150 bar on the cold side and $400 \text{ }^\circ\text{C}$ and 75 bar on the hot side. It should be pointed out that the CFD simulation for comparison with the correlations employs the constant thermophysical properties of CO₂, which are the

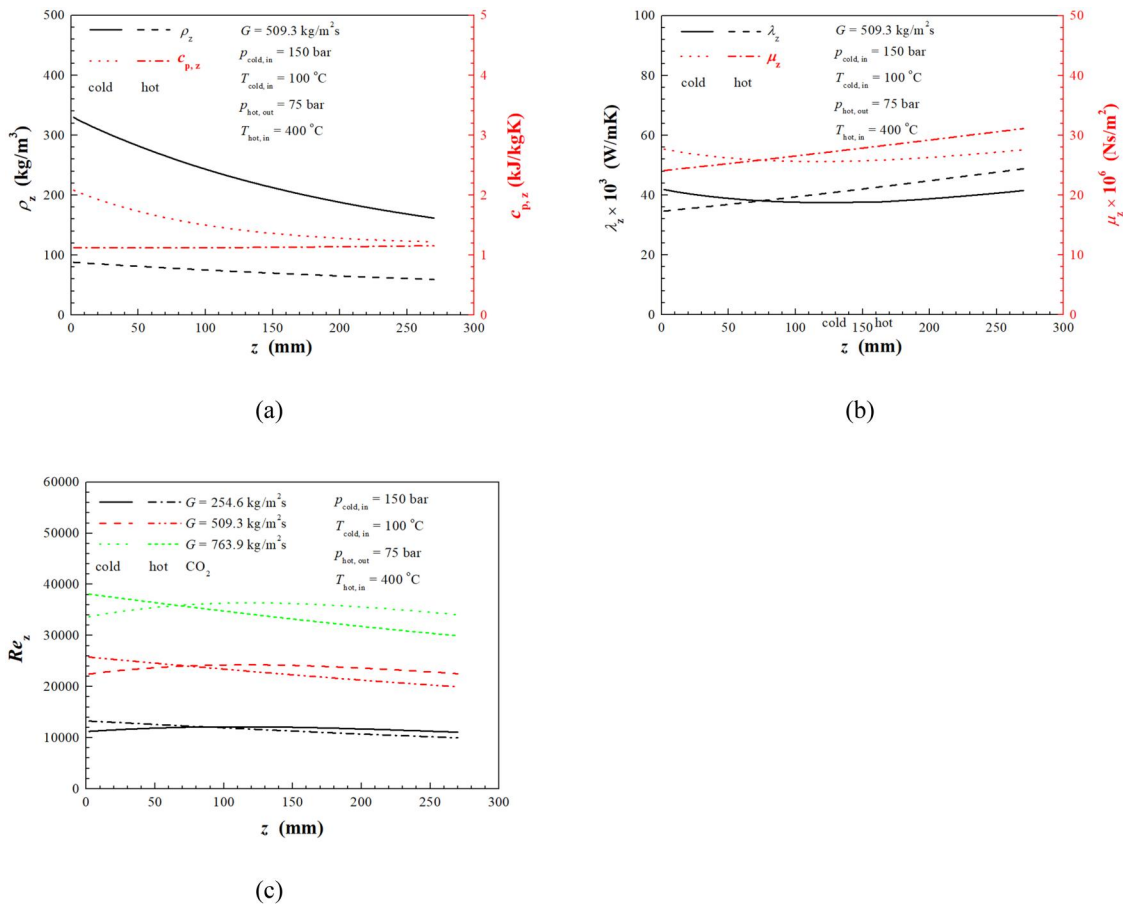


Figure 6. Local fluid thermophysical properties and Reynolds number. (a) Density and specific heat, (b) Thermal conductivity and dynamic viscosity, and (c) Reynolds number.

mass-average values obtained from the simulation with NIST real-gas thermophysical properties. As shown in Figure 4a, the results from the CFD simulations match very well the predictions from the Gnieliski correlation [36]. The Dittus-Boelter relationship [35] overpredicts the heat transfer coefficient on the hot and cold sides by approximately 6%. The larger differences at the cold and hot fluid entrances to the heat exchanger are mainly caused by the assumptions of uniform temperature and velocity at the entrances. As shown in Figure 4b, the pressure drop difference between the CFD results and the correlation predictions from the Blasius correlation [37] and Petukhov correlation [38] is less than 12%. The good agreements for both heat transfer and pressure drop data confirm the validity of the CFD modeling approach adopted.

Results and discussion

Local thermal performance

Figure 5 shows the local thermal performance for different mass fluxes, including the fluid temperature,

temperature difference between hot and cold sides and heat flux variation, as well as the local heat transfer coefficient and the corresponding Nusselt number. The temperature difference and local heat flux increase along the cold CO₂ flow direction. The heat transfer coefficient of cold CO₂ shows an obvious decrease along its flow direction, while the decrease of hot CO₂ is not that obvious. The Nusselt number declines along the flow direction on the cold side and increases on the hot side except the relatively short entrance region. The entrance region leads to much larger heat flux on the two ends of the heat exchanger due to the uniform temperature assumption, where the heat transfer coefficients and Nusselt number are also quite high. With the development of the thermal boundary layer, the heat transfer coefficient reduces quickly and then becomes stable along the flow direction. Increasing CO₂ mass flux leads to a significant increase in local heat flux and heat transfer coefficient, despite a comparably slight increase in temperature difference.

Since the CO₂ thermophysical properties have a significant influence on the local thermohydraulic

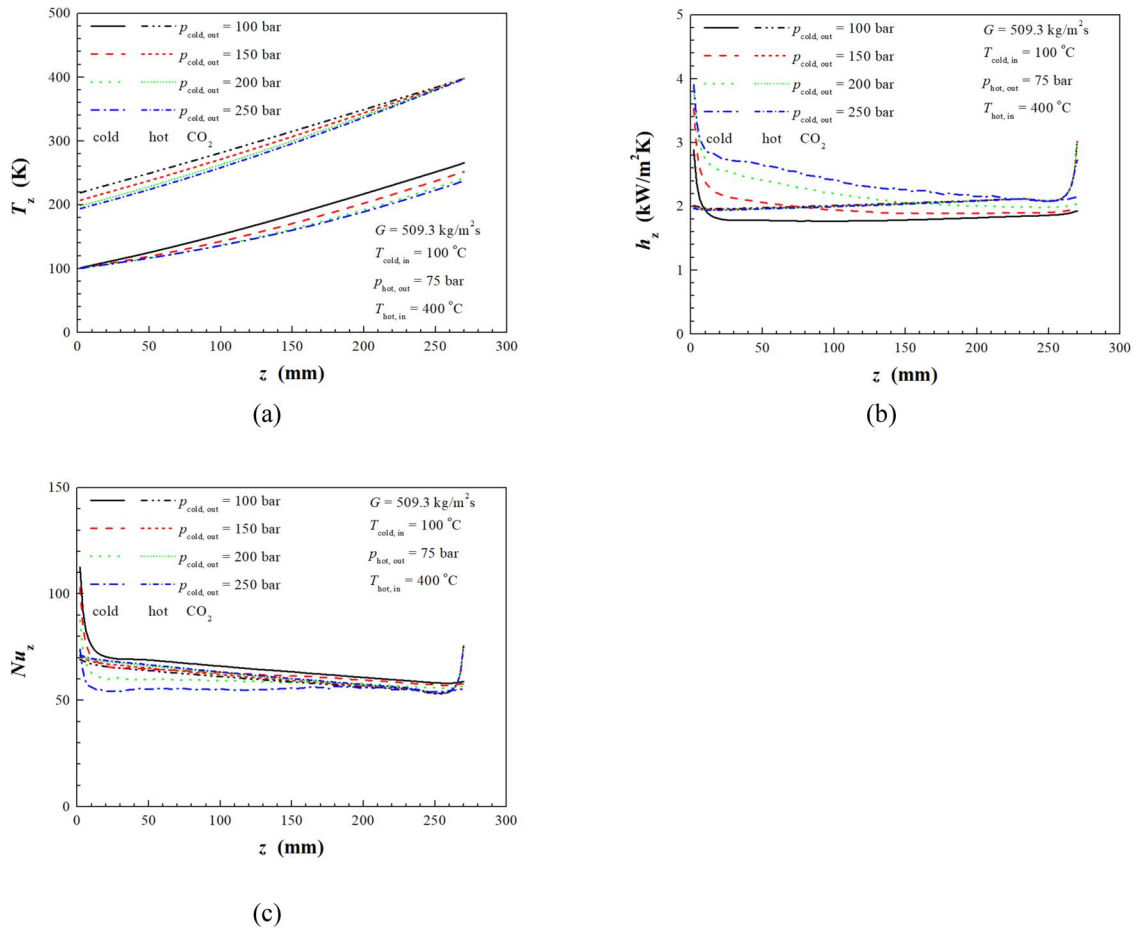


Figure 7. Local thermal performance for different pressures of cold CO_2 . (a) Fluid temperature, (b) Heat transfer coefficient, and (c) Nusselt number.

performance, Figure 6 shows the variations of CO_2 thermophysical properties along the flow direction. The local Reynolds number is also presented. The density of cold CO_2 drops from 332 kg/m^3 to 161 kg/m^3 along its flow direction, while that of the hot increases from 59 kg/m^3 to 88 kg/m^3 . The specific heat reduces largely from $2.103 \text{ kJ}/(\text{kg}\cdot\text{K})$ to $1.221 \text{ kJ}/(\text{kg}\cdot\text{K})$ along the cold flowing while drops only from $1.156 \text{ kJ}/(\text{kg}\cdot\text{K})$ to $1.125 \text{ kJ}/(\text{kg}\cdot\text{K})$ along the hot. The thermal conductivity and dynamic viscosity demonstrate very similar trends, both firstly going down slowly and then gently up on the cold side while keep dropping along the hot flowing. The thermal conductivity drops from $41.1 \times 10^{-3} \text{ W}/(\text{m}\cdot\text{K})$ to $37.5 \times 10^{-3} \text{ W}/(\text{m}\cdot\text{K})$ and then up to $41.6 \times 10^{-3} \text{ W}/(\text{m}\cdot\text{K})$ along the cold CO_2 flowing and drops from $48.9 \times 10^{-3} \text{ W}/(\text{m}\cdot\text{K})$ to $34.5 \times 10^{-3} \text{ W}/(\text{m}\cdot\text{K})$ along the hot. The dynamic viscosity reduces from $27.8 \times 10^{-6} \text{ Ns/m}^2$ to $25.6 \times 10^{-6} \text{ Ns}/(\text{m}^2\cdot\text{s})$ and then up to $27.6 \times 10^{-6} \text{ Ns/m}^2$ for the cold CO_2 and declines from $31.2 \times 10^{-6} \text{ Ns/m}^2$ to $24.1 \times 10^{-6} \text{ Ns/m}^2$ for the hot. The local Reynolds number correspondingly varies with the dynamic

viscosity, due to their inverse proportional relationship for the fixed mass flux and the hydraulic diameter.

Figure 7 shows the influence of cold CO_2 pressure on local thermal performance. A larger pressure brings about a smaller temperature rise of the cold fluid and a larger temperature drop of the hot fluid. This is mainly caused by the increased specific heat with increasing pressure. The pressure significantly impacts the heat transfer coefficient and Nusselt number of the cold CO_2 . A higher pressure, results in higher heat transfer coefficient but a decreased Nusselt number. This is mainly caused by the increased thermal conductivity with pressure. A higher pressure also leads to higher dynamic viscosity and thus a smaller Reynolds number and also reduces the Nusselt number. The cold CO_2 pressure has very little impact on the heat transfer from the hot side. As shown in Figure 8, increasing the inlet temperature of the cold CO_2 creates a substantial temperature drop in the hot CO_2 . The temperature drops are $252 \text{ }^\circ\text{C}$, $221 \text{ }^\circ\text{C}$, $194 \text{ }^\circ\text{C}$, $173 \text{ }^\circ\text{C}$ and $155 \text{ }^\circ\text{C}$, respectively with

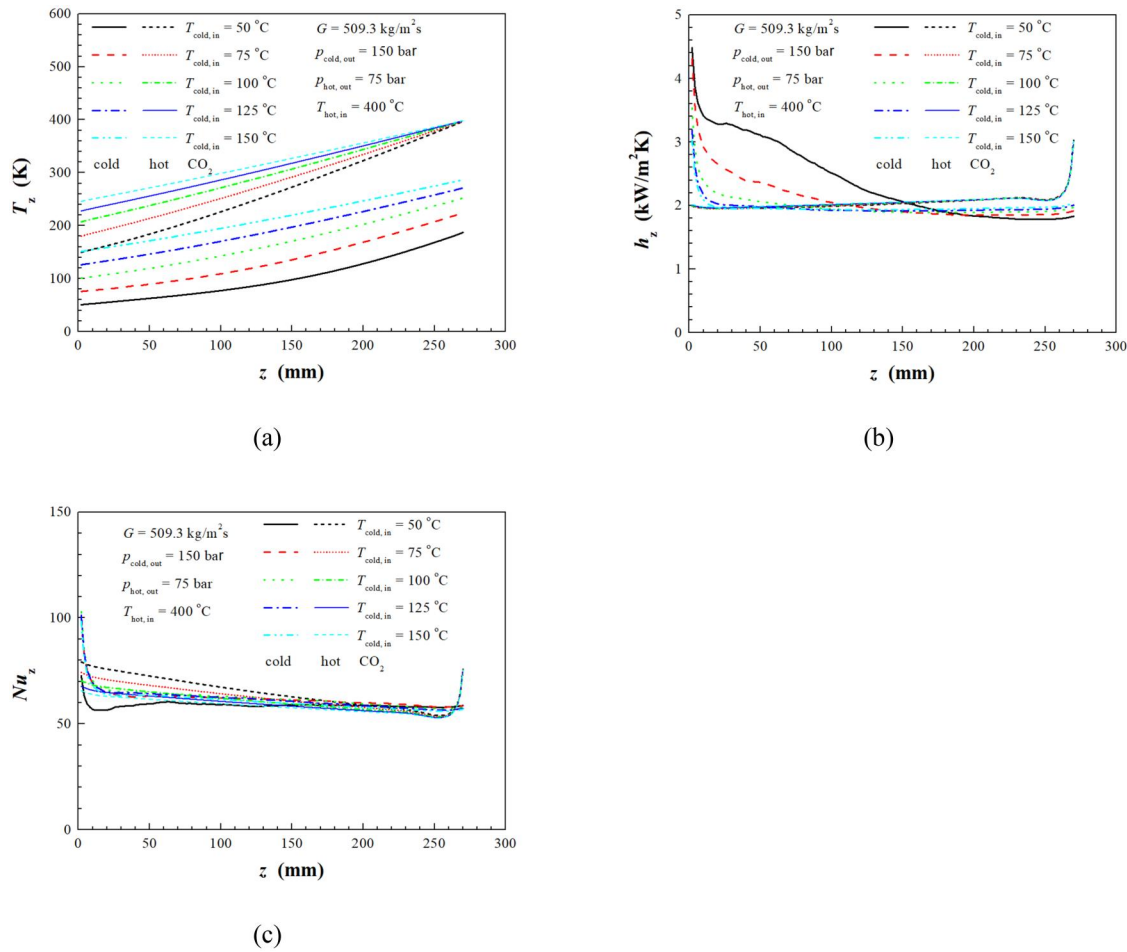


Figure 8. Local thermal performance for different temperatures of cold CO_2 . (a) Fluid temperature, (b) Heat transfer coefficient, and (c) Nusselt number.

the cold CO_2 inlet temperature $50 \text{ }^\circ\text{C}$, $100 \text{ }^\circ\text{C}$, $150 \text{ }^\circ\text{C}$, $200 \text{ }^\circ\text{C}$ and $250 \text{ }^\circ\text{C}$. The corresponding temperature rises on the cold side are $139 \text{ }^\circ\text{C}$, $151 \text{ }^\circ\text{C}$, $153 \text{ }^\circ\text{C}$, $147 \text{ }^\circ\text{C}$ and $137 \text{ }^\circ\text{C}$, respectively. The cold CO_2 temperature significantly impacts the heat transfer coefficient, especially in the case where the inlet temperature is $50 \text{ }^\circ\text{C}$ which is close to the pseudocritical region, and the thermophysical properties such as specific heat and thermal conductivity experience a wide variation with temperature. This leads to a higher local heat transfer coefficient compared to higher inlet temperatures, particularly in the first half of the heat exchanger. For the pressure of 150 bar , the pseudocritical temperature of CO_2 is $64.3 \text{ }^\circ\text{C}$. With the rapid increase of specific heat near the pseudocritical point, the heat transfer coefficient increases significantly reaching the peak near the pseudocritical temperature, and then quickly decreases. At the region away from the pseudocritical point, the heat transfer coefficient becomes insensitive to pressure and temperature variations. The influence on the local Nusselt number is not as significant as that on the heat

transfer coefficient, due to the reduction in the thermal conductivity close to the pseudocritical temperature and balances out the increase in the specific heat.

Figures 9 and 10 respectively demonstrate the influence of hot CO_2 pressure and temperature on the local thermal performance. With the hot CO_2 pressure increased from 75 bar to 150 bar , the difference of the outlet temperature of the cold CO_2 is less than $6 \text{ }^\circ\text{C}$ and that of the hot is less than $7 \text{ }^\circ\text{C}$, suggesting the hot CO_2 pressure has little impact on the local thermal performance. The increased pressure brings about variations in the thermophysical properties on the hot side and further increases the heat transfer coefficient, but the local Nusselt number has no obvious difference. The influence of the hot CO_2 temperature is more evident than the pressure as shown in Figure 10. A large hot CO_2 temperature results in a clearly larger temperature rise on the cold side, and these temperature variations significantly affect the local heat transfer of both the cold and hot CO_2 . The increased hot CO_2 temperature results in a lower local heat transfer coefficient and Nusselt number on the

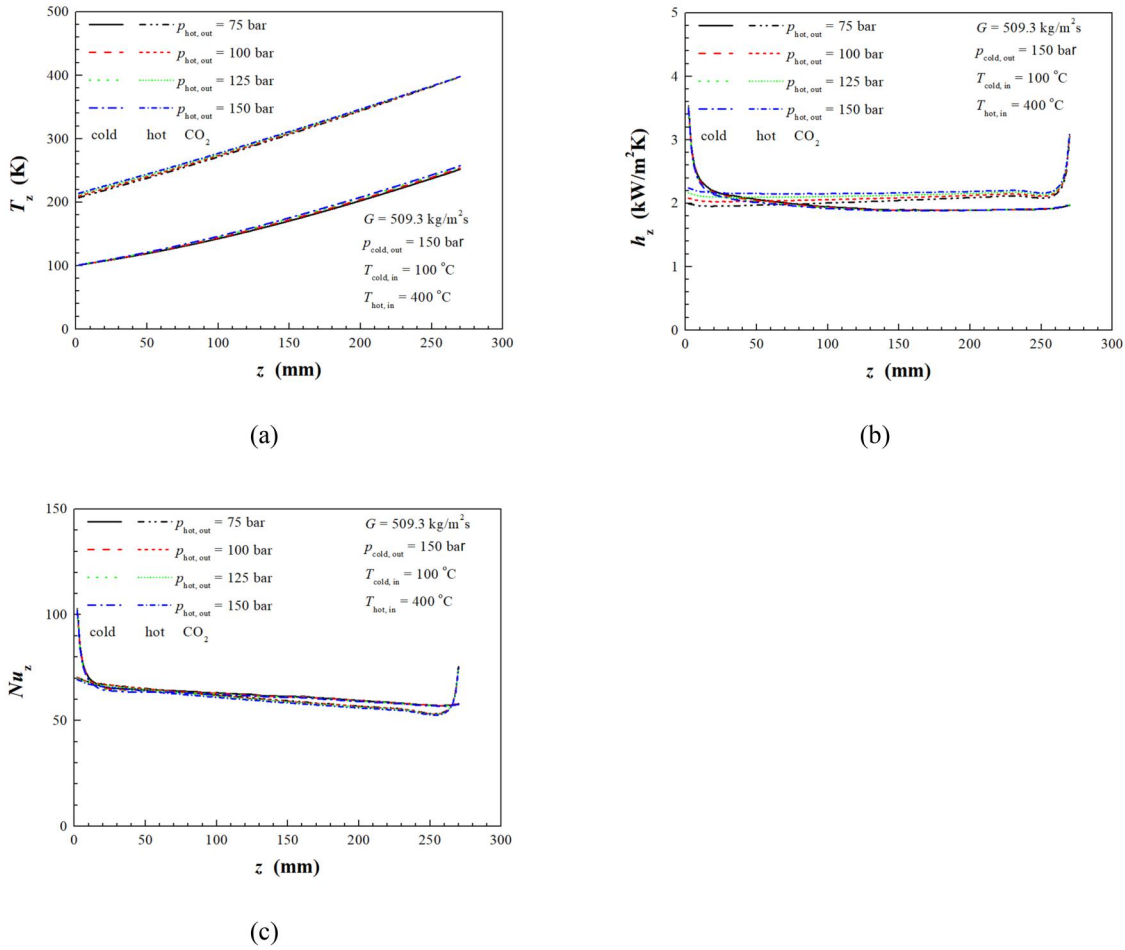


Figure 9. Local thermal performance for different pressures of hot CO₂. (a) Fluid temperature, (b) Heat transfer coefficient, and (c) Nusselt number.

cold side, while a higher local heat transfer coefficient but lower Nusselt number on the hot side. The lower Nusselt number on the hot side is mainly caused by thermal conductivity and partially by the decreased Reynolds number resulting from the increased dynamic viscosity. For example, the thermal conductivity increases from $34.0 \times 10^{-3} \text{ W/(m}\cdot\text{K)}$ to $48.9 \times 10^{-3} \text{ W/(m}\cdot\text{K)}$ as the temperature rises from $200 \text{ }^\circ\text{C}$ to $400 \text{ }^\circ\text{C}$ at pressure 75 bar and the corresponding dynamic viscosity increases from $24.1 \times 10^{-6} \text{ Ns/m}^2$ to $31.4 \times 10^{-6} \text{ Ns/m}^2$.

Local hydraulic performance

Figure 11 shows the influence of CO₂ mass flux on the local pressure and friction factor. The pressure decreases steadily along the flow direction on both cold and hot sides, the pressure drop on the hot side is much higher than that on the cold, and the increasing mass flux results in a larger local pressure drop. For the mass flux of $254.6 \text{ kg/(m}^2\cdot\text{s)}$, $509.3 \text{ kg/(m}^2\cdot\text{s)}$, and $763.9 \text{ kg/(m}^2\cdot\text{s)}$, the pressure drop shows 1.17,

3.76, and 7.65 kPa on the cold side, and 2.46, 8.34 and 17.16 kPa on the hot. As shown in Figure 11b, the friction factor on the hot side is much lower than that on the cold, and a larger mass flux leads to a lower friction factor. Corresponding to the entrance region, the friction factor shows a sharp decline along the developing of the boundary layer. After that, the friction factor remains comparably stable and just a little drop along the flow direction for both hot and cold CO₂.

Figures 12 and 13, respectively, show the influence of the cold CO₂ pressure and temperature. Increasing pressure largely reduces the pressure drop on the cold side. For the inlet pressure 100, 150, 200, and 250 bar, the pressure drop is 5.95, 3.76, 2.74, and 2.24 kPa on the cold side. The corresponding pressure drop on the hot side is 8.61, 8.34, 8.11 and 7.95 kPa. The increased inlet pressure enlarges the friction factor on the cold side but not on the hot side. The decrease of cold CO₂ temperature leads to less pressure drop on both cold and hot sides. The decreased temperature on both sides brings about a larger fluid density, which

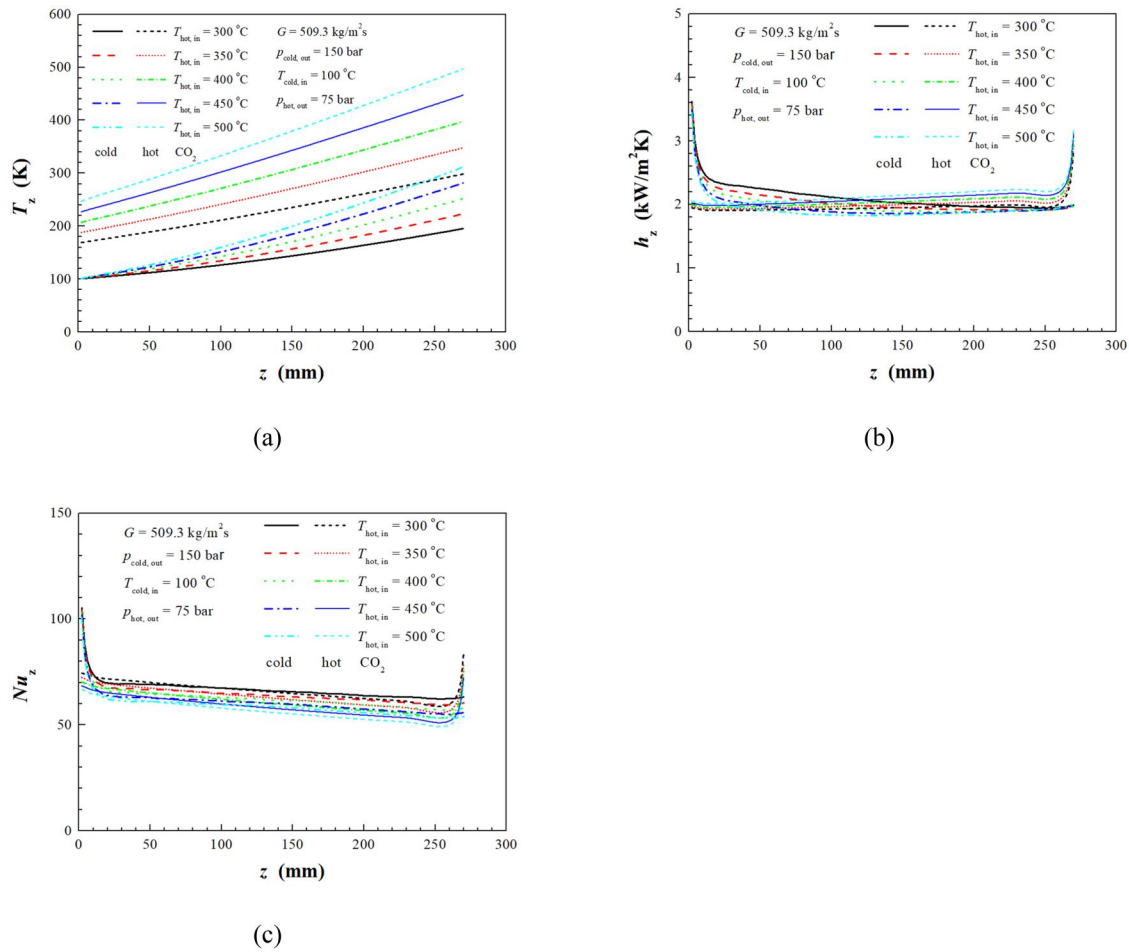


Figure 10. Local thermal performance for different temperatures of hot CO₂. (a) Fluid temperature, (b) Heat transfer coefficient, and (c) Nusselt number.

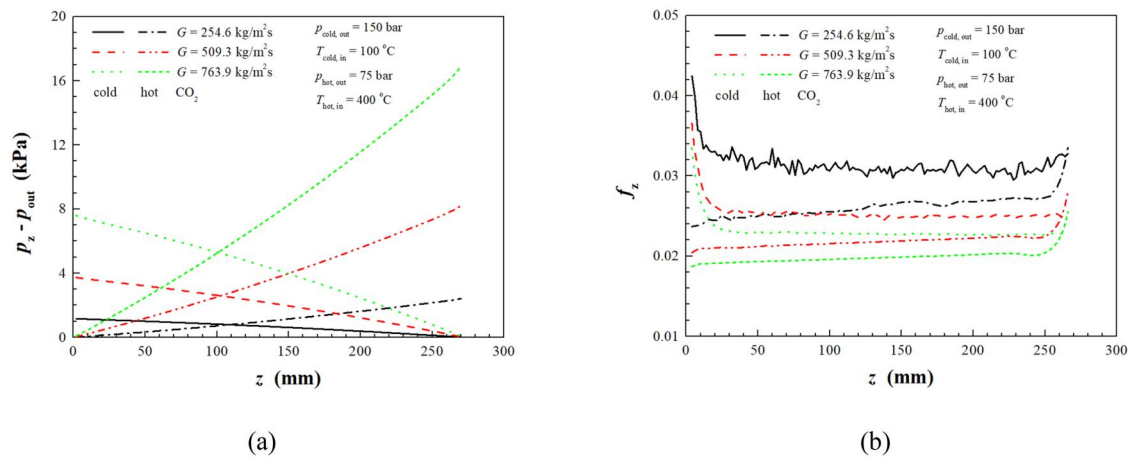


Figure 11. Local hydraulic performance for different mass fluxes. (a) Pressure drop and (b) Friction factor.

reduces the pressure drop largely. For the inlet temperature drops from 150°C to 50°C , the pressure drops decline from 4.27 kPa to 2.75 kPa on the cold side and from 9.09 kPa to 7.12 kPa on the hot. Decreasing cold CO₂ temperature leads to an increased friction factor on the cold side and a decreased on the hot.

As shown in Figure 14, the hot CO₂ inlet pressure seriously impacts its own pressure drop. For the hot pressure of 75, 100, 125, and 150 bar, the pressure drops on hot side are 8.34, 6.28, 5.02, and 4.21 kPa, respectively. As shown in Figure 15, the increased hot CO₂ temperature results in obviously larger pressure drop on both sides and just a slight influence on the

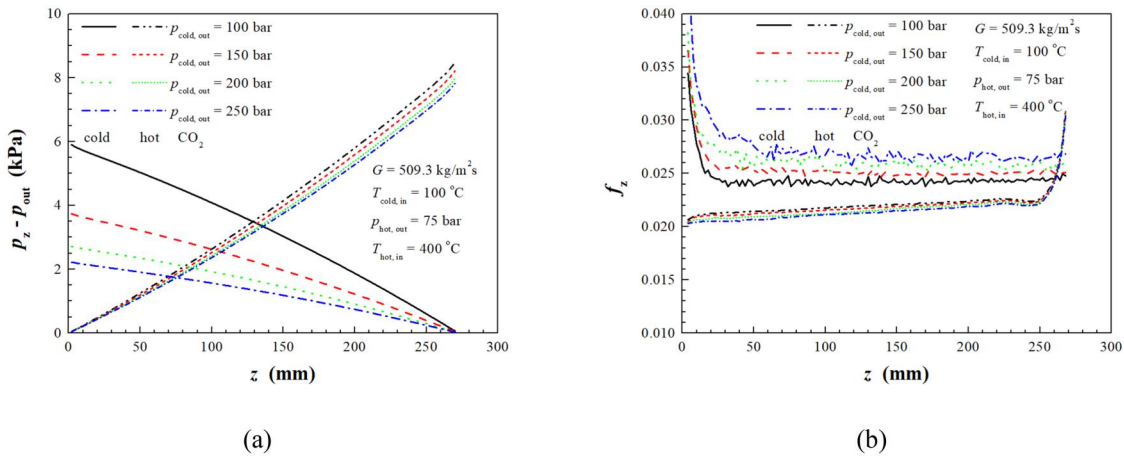


Figure 12. Local hydraulic performance for different pressures of cold CO₂. (a) Pressure drop and (b) Friction factor.

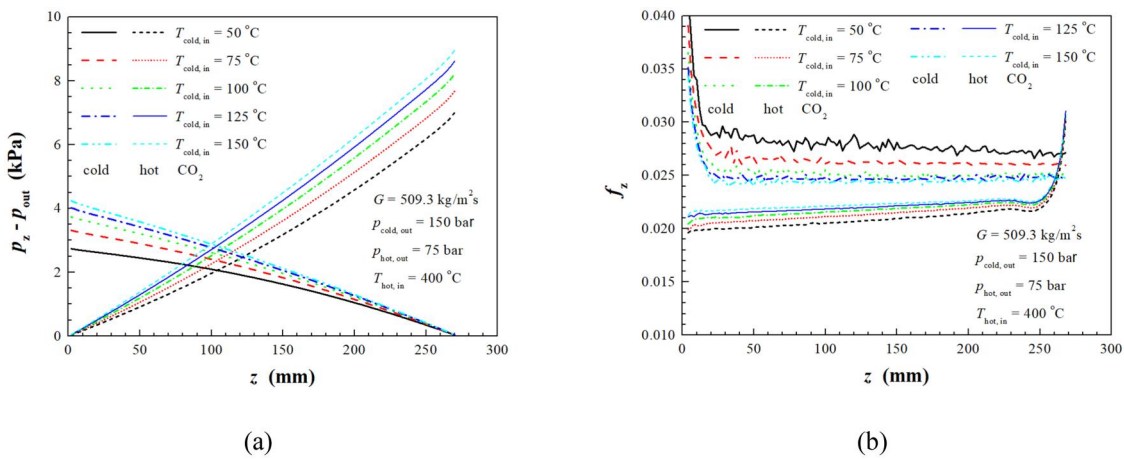


Figure 13. Local hydraulic performance for different temperatures of cold CO₂. (a) Pressure drop and (b) Friction factor.

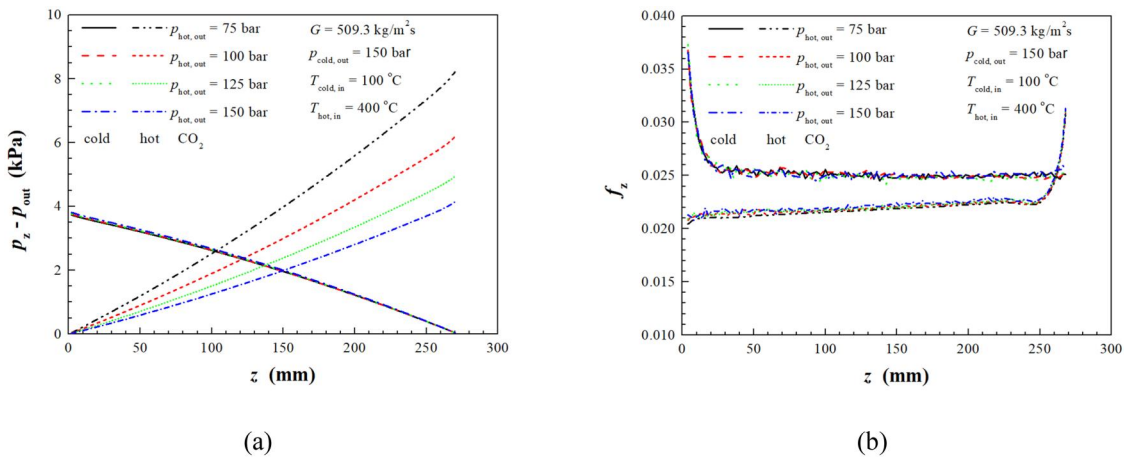


Figure 14. Local hydraulic performance for different pressures of hot CO₂. (a) Pressure drop and (b) Friction factor.

friction factor. For the inlet temperature rises from $300 \text{ }^\circ\text{C}$ to $500 \text{ }^\circ\text{C}$, the pressure drop goes up from 3.19 kPa to 4.32 kPa on the cold side and from 7.11 kPa to 9.54 kPa on the hot, respectively.

Average thermal performance

As illustrated by Figure 16, the larger mass flux improves the heat transfer coefficient. Consequently, the Nusselt number rises with the increased Reynolds

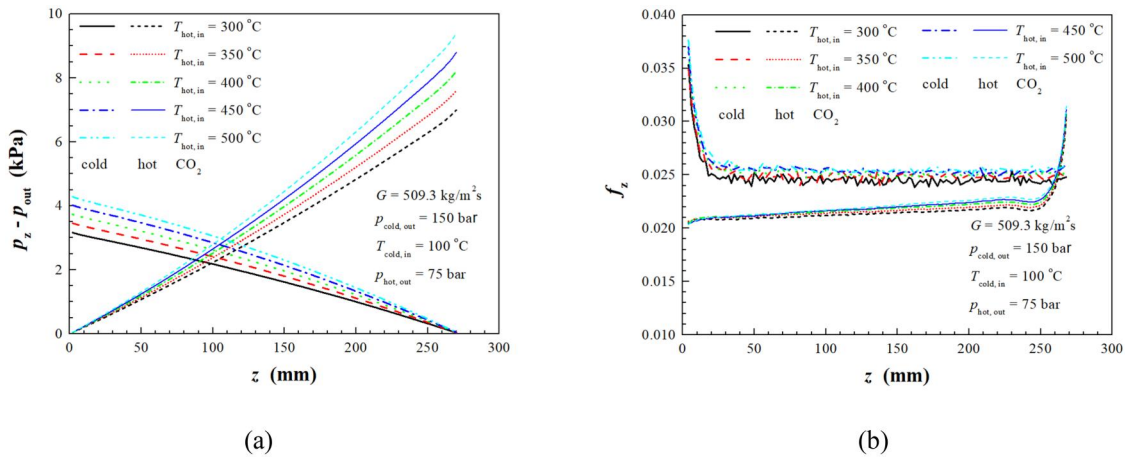


Figure 15. Local hydraulic performance for different temperatures of hot CO₂. (a) Pressure drop and (b) Friction factor.

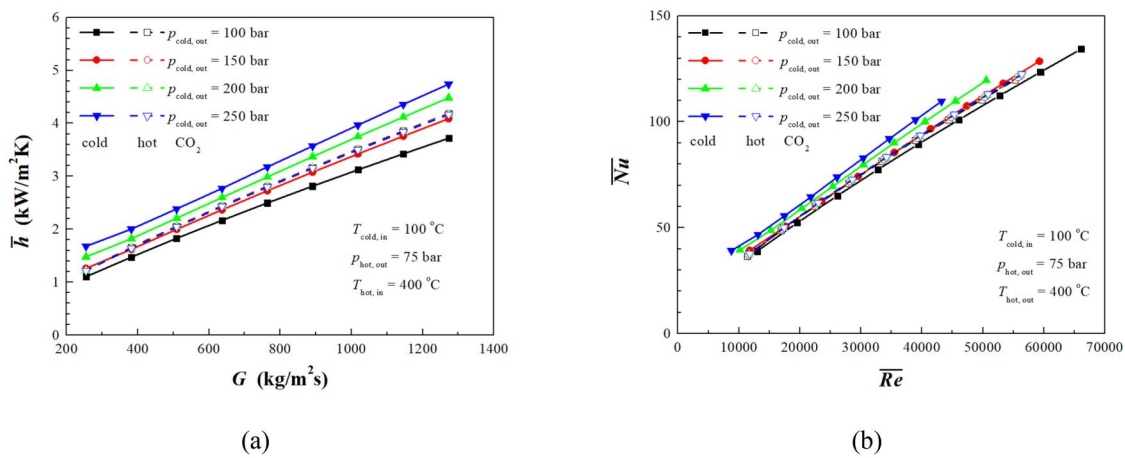


Figure 16. Average thermal performance for different pressures of the cold CO₂. (a) Heat transfer coefficient and (b) Nusselt number.

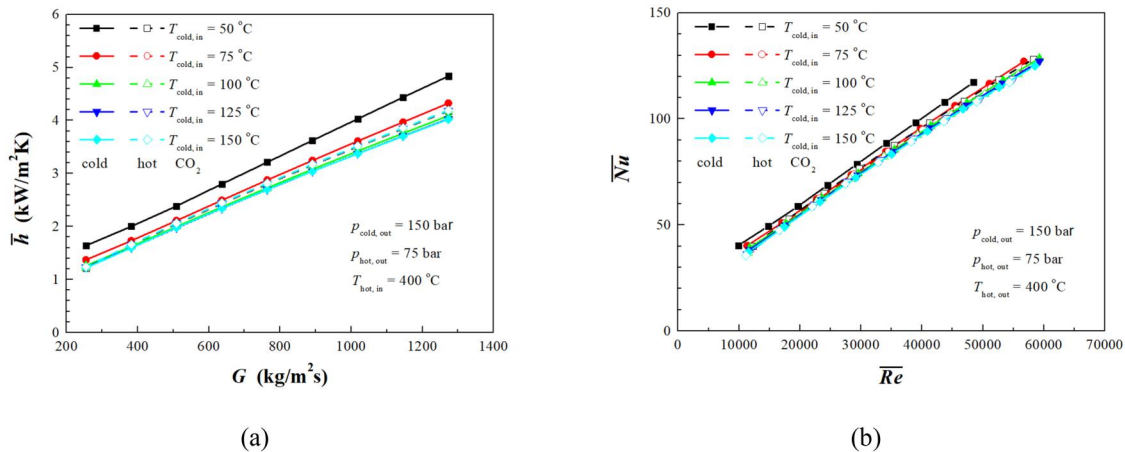


Figure 17. Average thermal performance for different temperatures of cold CO₂. (a) Heat transfer coefficient and (b) Nusselt number.

number. As shown in Figure 16, increasing cold CO₂ pressure results in a higher heat transfer coefficient and Nusselt number, and lower Reynolds number on the cold side. Figure 17 presents the influence of cold

CO₂ temperature on average thermal performance. The case with CO₂ temperature 50 °C gives higher heat transfer coefficient than the others on the cold side. As mentioned in Figure 8, the cold CO₂ goes

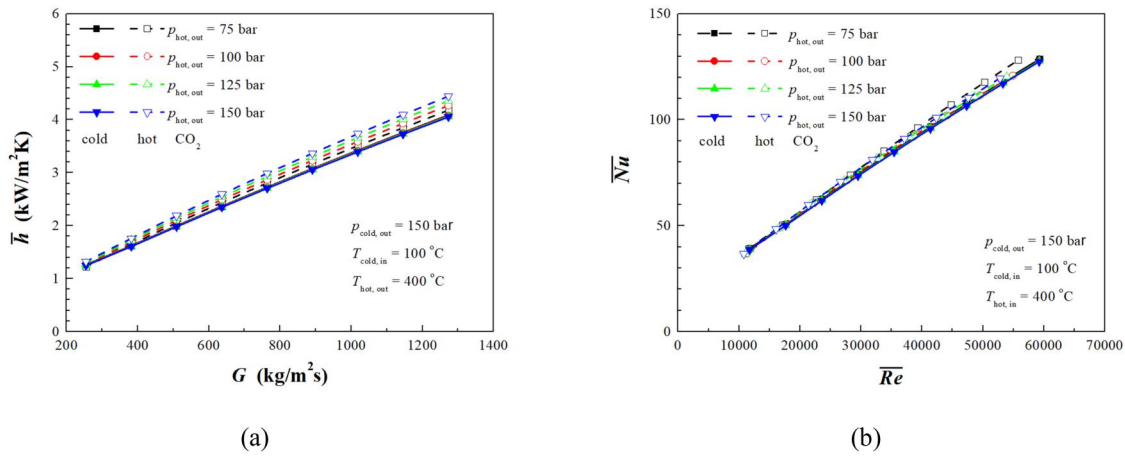


Figure 18. Average thermal performance for different pressures of hot CO₂. (a) Heat transfer coefficient and (b) Nusselt number.

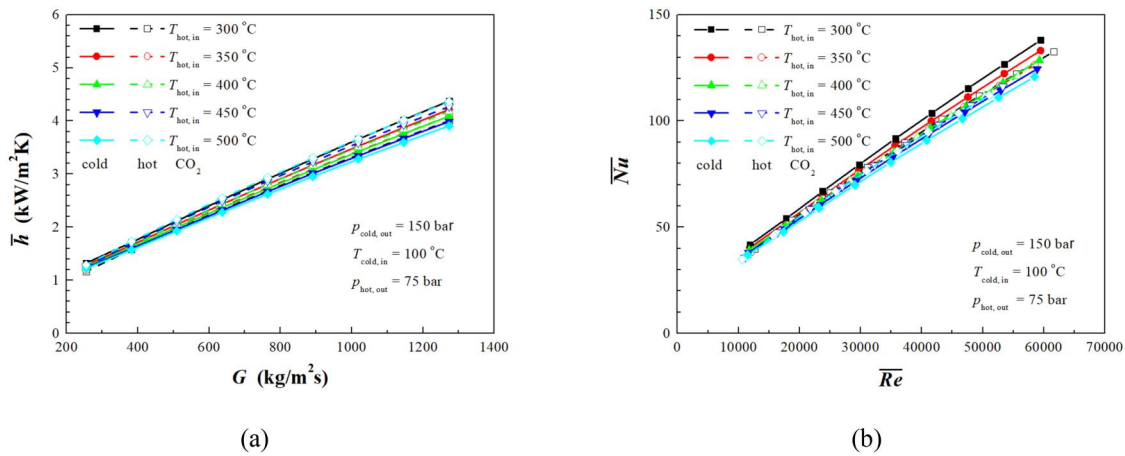


Figure 19. Average thermal performance for different temperatures of hot CO₂. (a) Heat transfer coefficient and (b) Nusselt number.

through the region near the pseudocritical point. Correspondingly, the heat transfer coefficient increases rapidly, reaches a peak near the pseudocritical temperature, and then decreases. This phenomenon significantly enhances heat transfer. The pressure and temperature of cold CO₂ have no evident impact on the hot side.

As shown in Figure 18, the larger hot CO₂ pressure causes a notably higher heat transfer coefficient on its own side for a fixed mass flux, while the increased Nusselt number is not notable due to the decreased Reynolds number. The increasing pressure brings about the rise of dynamic viscosity and further lessens the Reynolds number. The hot CO₂ pressure shows negligible impact on the average thermal performance on the cold side. As demonstrated in Figure 19, the hot CO₂ temperature affects the thermal performance on both sides. Increasing temperature brings about larger heat transfer coefficient on the hot side but lower on the cold, while decreased Nusselt number on the cold side and slightly increased on the hot.

To clarify the influence of operation parameters on thermal performance, Figure 20 demonstrates the variation of overall heat transfer rate under the different operating conditions. Decreased cold temperatures and increased hot temperatures lead to a significant increase in the heat transfer rate, owing to the obviously larger temperature difference between the two sides. The pressure on the cold side shows a significant influence on the heat transfer rate, while the pressure on the hot side does not.

Average hydraulic performance

Figures 21 and 22 demonstrate the impact of cold CO₂ pressure and temperature on the average hydraulic performance. An increase in mass flux results in significantly increased pressure drop and largely decreased friction factor on both sides. As shown in Figure 21, increasing pressure of cold CO₂ leads to much higher pressure drop on the cold side, mostly caused by the enlarged fluid density by

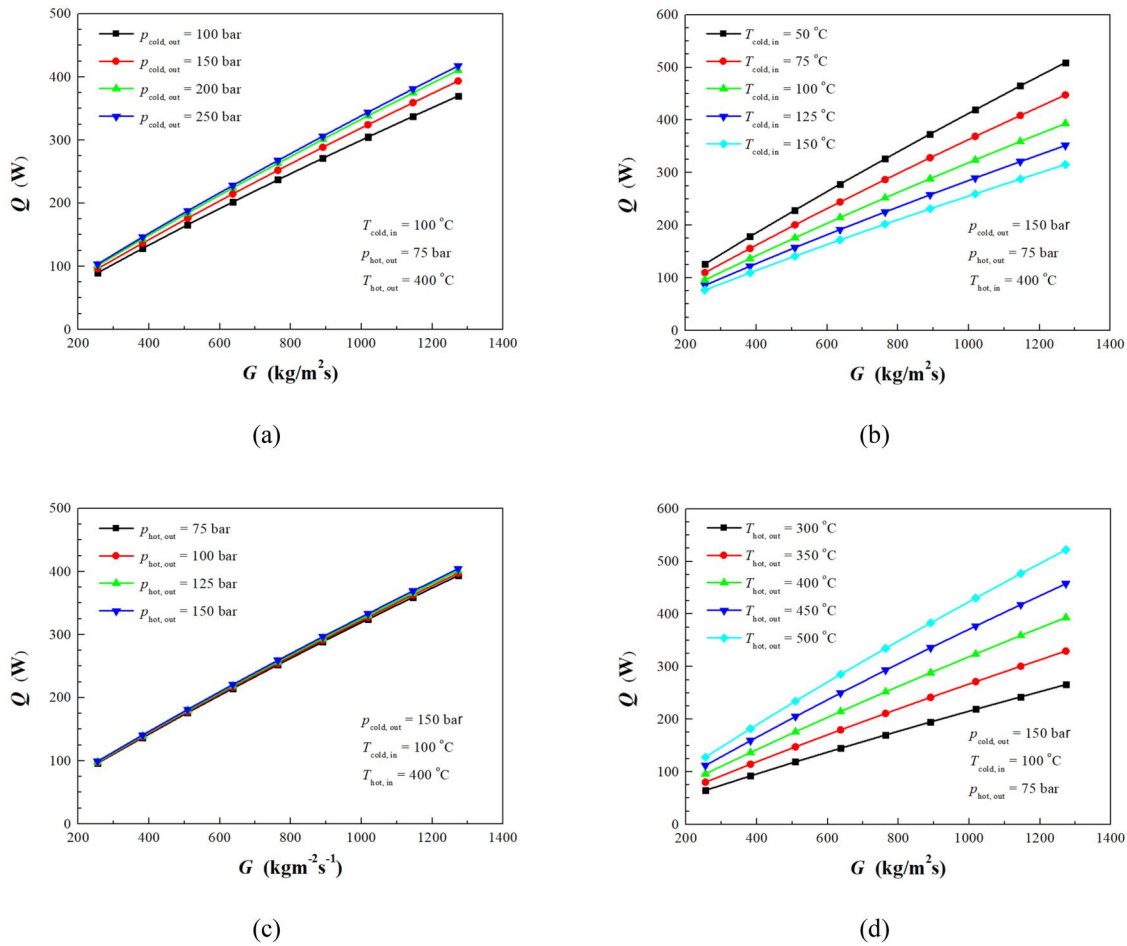


Figure 20. Influence of operating conditions on overall heat transfer rate. (a) Pressures of cold CO₂, (b) temperatures of cold CO₂, (c) pressures of hot CO₂, and (d) temperatures of hot CO₂.

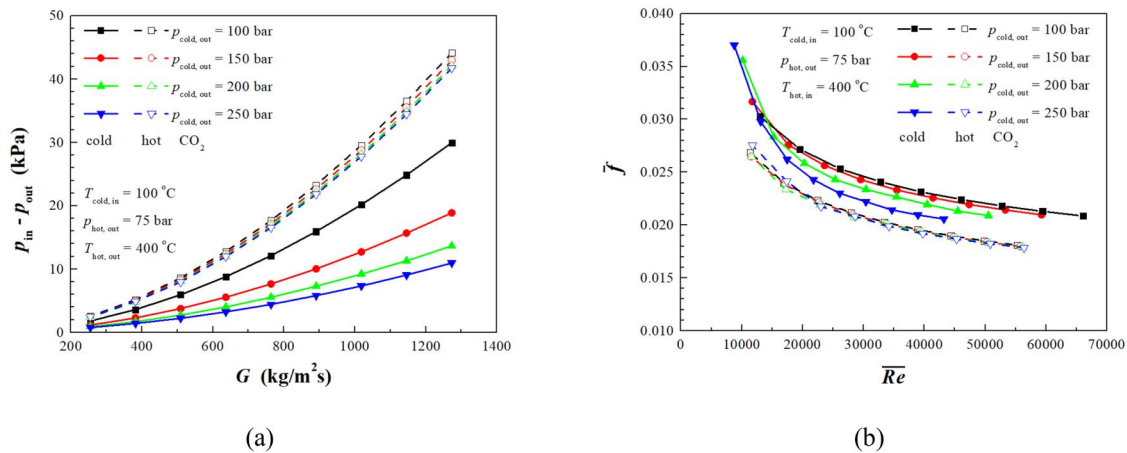


Figure 21. Average hydraulic performance for different pressures of cold CO₂. (a) Pressure drop and (b) Friction factor.

pressure. For example, the CO₂ density jumps from 145.6 kg/m^3 to 415.5 kg/m^3 with pressure from 100 bar to 250 bar at fixed temperature 150°C . The increasing cold CO₂ pressure slightly declines the pressure drop on the hot side. The increase in cold CO₂ pressure clearly drops the friction factor and broadens their

difference on the cold side. The cold CO₂ temperature shows more significant impacts. Decreasing temperature largely drops the pressure drop on both sides. The reduction of friction factor on hot side is not as obvious as the pressure drop due to the increased Reynolds number.

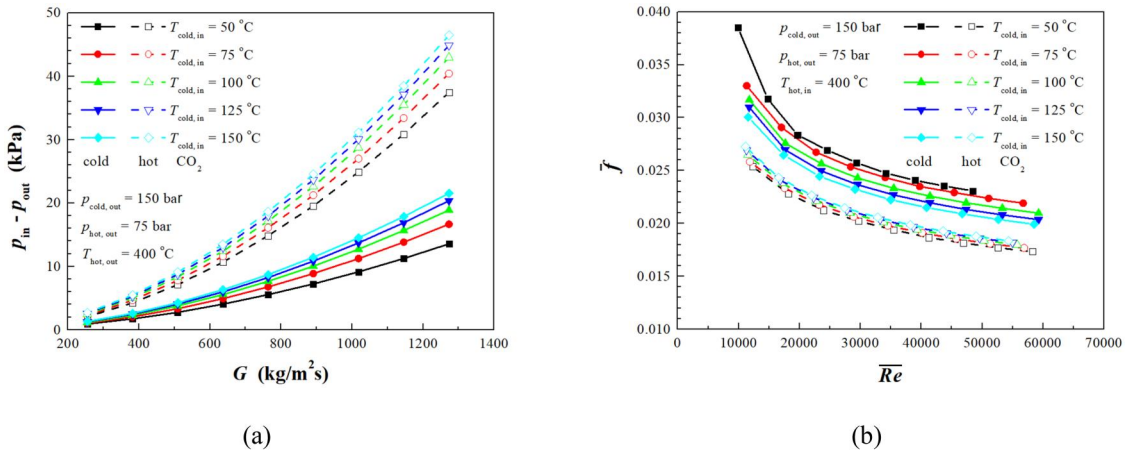


Figure 22. Average hydraulic performance for different temperatures of cold CO₂. (a) Pressure drop and (b) Friction factor.

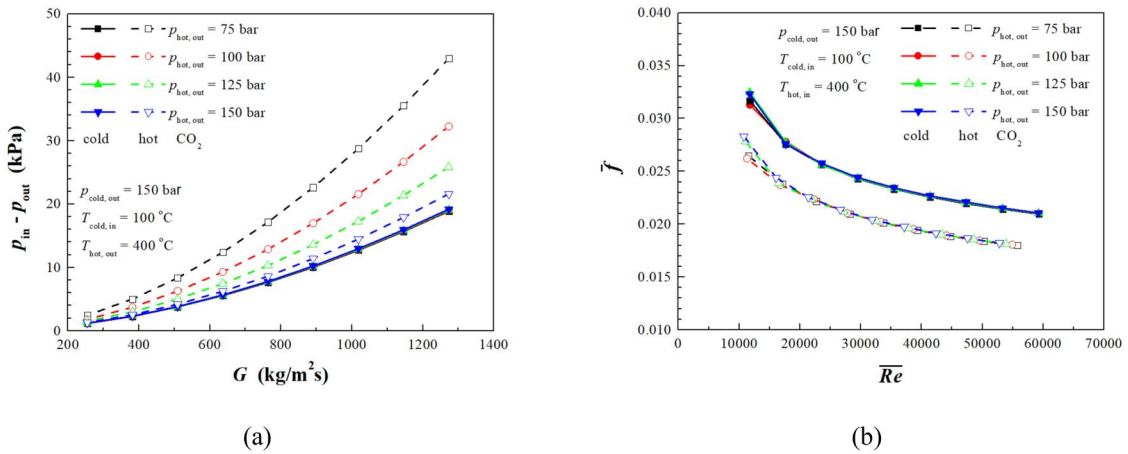


Figure 23. Average hydraulic performance for different pressures of hot CO₂. (a) Pressure drop and (b) Friction factor.

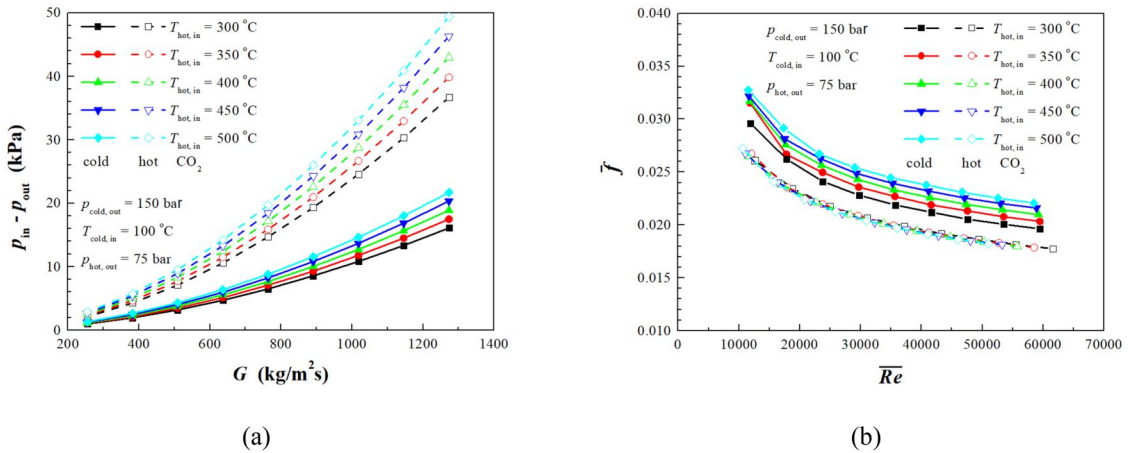


Figure 24. Average hydraulic performance for different temperatures of hot CO₂. (a) Pressure drop and (b) Friction factor.

Figures 23 and 24 show the variations of pressure drop and friction factor with the hot CO₂ pressure and temperature. The increased pressure significantly reduces the pressure drop on its own side but has no influence on the cold side. The friction factor with Reynolds number shows little dependence on the hot

CO₂ pressure. The increase in temperature enlarges the pressure drop much on its own side but has no clear influence on the variation of friction factor with Reynolds number, while bringing about obviously larger pressure drop and friction factor on the cold side.

Conclusions

A three-dimensional numerical model was developed to investigate the thermohydraulic performance of sCO₂ flowing in a printed circuit heat exchanger. The impact of operating parameters on local and average heat transfer and pressure drop was investigated for both the hot and cold CO₂ as well as their interaction. The information provided in this article should be useful in the design optimization of optimized recuperative heat exchangers for sCO₂ power generation applications. The major conclusions can be summarized as follows:

- The entrance region leads to a much larger heat flux on the two ends of the heat exchanger, higher heat transfer coefficients and Nusselt number as well as a larger friction factor for both hot and cold CO₂. With the development of thermal and hydraulic boundary layers in the entrance region, the heat transfer coefficient and friction factor reduce quickly and then become stable along the flow direction. Increasing CO₂ mass flux leads to a significant increase in heat flux and heat transfer coefficient and a slight increase in temperature difference between hot and cold CO₂. The larger mass flux leads to a larger pressure drop but a lower friction factor on both sides.
- Due to the increased thermal conductivity and the increased dynamic viscosity with increasing pressure, increasing cold CO₂ pressure results in a higher heat transfer coefficient but lower Nusselt number, as well as lower pressure drop even though the friction factor increases on the cold side. The cold side CO₂ temperature has a significant influence on heat transfer on the cold side, particularly for the lower inlet temperatures which lead to much higher heat transfer coefficient in the first half part of the heat exchanger due to the temperature being close to the pseudocritical point. The cold CO₂ temperature has no obvious impact on the heat transfer coefficient on the hot side but the Nusselt number changes noticeably due to the thermal conductivity variation with hot CO₂ temperature. Lower cold CO₂ temperatures lead to the reduction of pressure drop on both sides.
- Increasing the hot CO₂ pressure leads to a slightly higher heat transfer coefficient, a slightly lower Nusselt number, but significantly reduced pressure drops on both sides. The hot CO₂ pressure has little impact on the thermal and hydraulic performance on the cold side. Increasing the hot CO₂ temperature increases the heat transfer coefficient on the hot side but causes a reduction in the heat

transfer coefficient on the cold side. The increase in hot CO₂ temperature leads to a higher pressure drop on both sides of the heat exchanger.

Acknowledgements

The work presented in this article was supported by a number of funders as follows: (i) The Engineering and Physical Sciences Research Council (EPSRC) of the UK under research grants EP/P004636/1—OPTMIN, and EP/V001795/1—SCOTWOHR; (ii) the European Union's Horizon 2020 research and innovation programme under grant agreement No. 680599—I-ThERM and Grant Agreement No. 101022831—CO2OLHEAT. The authors would like to acknowledge the financial support received from the funders and industry partners. All data used are in the article but if any additional information is required it can be obtained by contacting the corresponding author.

Disclosure statement

No potential conflict of interest was reported by the authors.

Notes on contributors



Lei Chai is a research fellow at the Institute of Energy Futures, Brunel University London. He received his BSc degree in oil and gas storage and transportation engineering in 2007 from the China University of Petroleum (East China) and his PhD degree in thermal energy engineering in 2012 from Beijing University of

Technology. He has published over sixty international journals and conference papers. His research interests are in the field of CO₂ power and refrigeration systems, energy storage devices and systems, heat transfer enhancement, and novel heat exchangers.



Savvas A. Tassou is the Director of the Institute of Energy Futures and the Director of the Center for Sustainable Energy Use in Food Chains, Brunel University London. He has over 30 years research experience in the area of thermal and energy engineering, covering heating and cooling systems, including heat pump and refrigeration technologies. More recently, his research has also extended to waste heat recovery from industrial processes and waste heat-to-power conversion using innovative heat exchangers and sCO₂ heat-to-power cycles.

ORCID

Lei Chai  <http://orcid.org/0000-0002-1293-0833>

References

- [1] L. Cheng and G. Xia, "Progress and prospects for research and technology development of supercritical CO₂ thermal conversion systems for power, energy storage, and waste heat recovery," *Heat Transfer Eng.*, pp. 1–18, 2023. DOI: [10.1080/01457632.2023.2282765](https://doi.org/10.1080/01457632.2023.2282765).
- [2] L. Chai and S. A. Tassou, "Performance analysis of heat exchangers and integrated supercritical CO₂ Brayton cycle for varying heat carrier, cooling and working fluid flow rates," *Heat Transfer Eng.*, vol. 44, no. 16–18, pp. 1498–1518, 2023. DOI: [10.1080/01457632.2022.2140640](https://doi.org/10.1080/01457632.2022.2140640).
- [3] K. Brun, P. Friedman, and R. Dennis, editors, *Fundamentals and Applications of Supercritical Carbon Dioxide (sCO₂) Based Power Cycles*, 1st ed., Woodhead Publishing, Cambridge, UK, 2017.
- [4] M. T. White, G. Bianchi, L. Chai, S. A. Tassou and A. I. Sayma, "Review of supercritical CO₂ technologies and systems for power generation," *Appl. Therm. Eng.*, vol. 185, pp. 116447, Feb. 2021. DOI: [10.1016/j.applthermaleng.2020.116447](https://doi.org/10.1016/j.applthermaleng.2020.116447).
- [5] L. Chai and S. A. Tassou, "Recent progress on high temperature and high pressure heat exchangers for supercritical CO₂ power generation and conversion systems," *Heat Transfer Eng.*, vol. 44, no. 21–22, pp. 1950–1968, 2023. DOI: [10.1080/01457632.2022.2164683](https://doi.org/10.1080/01457632.2022.2164683).
- [6] Q. Li, G. Flamant, X. Yuan, P. Neveu and L. Luo, "Compact heat exchangers: a review and future applications for a new generation of high temperature solar receivers," *Renew. Sustain Energy Rev.*, vol. 15, no. 9, pp. 4855–4875, Dec. 2011. DOI: [10.1016/j.rser.2011.07.066](https://doi.org/10.1016/j.rser.2011.07.066).
- [7] L. Chai and S. A. Tassou, "A review of printed circuit heat exchangers for helium and supercritical CO₂ Brayton cycles," *Therm. Sci. Eng. Prog.*, vol. 18, pp. 100543, Aug. 2020. DOI: [10.1016/j.tsep.2020.100543](https://doi.org/10.1016/j.tsep.2020.100543).
- [8] L. Cheng, K. Wang, G. Xia and A. J. Ghajar, "Advanced heat transfer technologies: fundamentals and applications," *Heat Transfer Eng.*, vol. 44, no. 21–22, pp. 1947–1949, Jan. 2023. DOI: [10.1080/01457632.2022.2164676](https://doi.org/10.1080/01457632.2022.2164676).
- [9] A. Kruiženga, *et al.*, "Heat transfer of supercritical carbon dioxide in printed circuit heat exchanger geometries," *J. Therm. Sci. Eng. Appl.*, vol. 3, no. 3, pp. 31002, Sep. 2011. DOI: [10.1115/1.4004252](https://doi.org/10.1115/1.4004252).
- [10] A. Kruiženga, H. Li, M. Anderson and M. Corradini, "Supercritical carbon dioxide heat transfer in horizontal semicircular channels," *ASME J. Heat Transf.*, vol. 134, no. 8, pp. 81802, Aug. 2012. DOI: [10.1115/1.4006108](https://doi.org/10.1115/1.4006108).
- [11] H. Li, *et al.*, "Development of a new forced convection heat transfer correlation for CO₂ in both heating and cooling modes at supercritical pressures," *Int. J. Therm. Sci.*, vol. 50, no. 12, pp. 2430–2442, Dec. 2011. DOI: [10.1016/j.ijthermalsci.2011.07.004](https://doi.org/10.1016/j.ijthermalsci.2011.07.004).
- [12] K. Nikitin, Y. Kato and L. Ngo, "Experimental and numerical study of printed circuit heat exchanger performance in carbon dioxide experimental loop," Presented at Proceedings of 6th Gustav Lorentzen Natural Working Fluids Conf., Glasgow, UK, August 29–September 1, 2004.
- [13] K. Nikitin, Y. Kato and L. Ngo, "Printed circuit heat exchanger thermal–hydraulic performance in supercritical CO₂ experimental loop," *Int. J. Refrig.*, vol. 29, no. 5, pp. 807–814, Aug. 2006. DOI: [10.1016/j.ijrefrig.2005.11.005](https://doi.org/10.1016/j.ijrefrig.2005.11.005).
- [14] K. Nikitin, Y. Kato and T. Ishizuka, "Experimental thermal-hydraulics comparison of microchannel heat exchangers with zigzag channels and S-shaped fins for gas turbine reactors," presented at Proc. of Fifteenth International Conference on Nuclear Engineering, Nagoya, Japan, April 22–26, 2007.
- [15] T. L. Ngo, Y. Kato, K. Nikitin and T. Ishizuka, "Heat transfer and pressure drop correlations of microchannel heat exchangers with S-shaped and zigzag fins for carbon dioxide cycles," *Exp. Therm. Fluid Sci.*, vol. 32, no. 2, pp. 560–570, Nov. 2007. DOI: [10.1016/j.expthermflusci.2007.06.006](https://doi.org/10.1016/j.expthermflusci.2007.06.006).
- [16] D. E. Kim, M. H. Kim, J. E. Cha and S. O. Kim, "Numerical investigation on thermal–hydraulic performance of new printed circuit heat exchanger model," *Nucl. Eng. Des.*, vol. 238, no. 12, pp. 3269–3276, Dec. 2008. DOI: [10.1016/j.nucengdes.2008.08.002](https://doi.org/10.1016/j.nucengdes.2008.08.002).
- [17] S.-M. Lee and K.-Y. Kim, "Optimization of zigzag flow channels of a printed circuit heat exchanger for nuclear power plant application," *J. Nucl. Sci. Technol.*, vol. 49, no. 3, pp. 343–351, 2012. DOI: [10.1080/00223131.2012.660012](https://doi.org/10.1080/00223131.2012.660012).
- [18] S.-M. Lee and K.-Y. Kim, "A parametric study of the thermal-hydraulic performance of a zigzag printed circuit heat exchanger," *Heat Transfer Eng.*, vol. 35, no. 13, pp. 1192–1200, 2014. DOI: [10.1080/01457632.2013.870004](https://doi.org/10.1080/01457632.2013.870004).
- [19] S.-M. Lee and K.-Y. Kim, "Multi-objective optimization of arc-shaped ribs in the channels of a printed circuit heat exchanger," *Int. J. Therm. Sci.*, vol. 94, pp. 1–8, Aug. 2015. DOI: [10.1016/j.ijthermalsci.2015.02.006](https://doi.org/10.1016/j.ijthermalsci.2015.02.006).
- [20] S. G. Kim, Y. Lee, Y. Ahn and J. I. Lee, "CFD aided approach to design printed circuit heat exchangers for supercritical CO₂ Brayton cycle application," *Ann. Nucl. Energy*, vol. 92, pp. 175–185, Jun. 2016. DOI: [10.1016/j.anucene.2016.01.019](https://doi.org/10.1016/j.anucene.2016.01.019).
- [21] S. Y. Lee, B. G. Park and J. T. Chung, "Numerical studies on thermal hydraulic performance of zigzag-type printed circuit heat exchanger with inserted straight channels," *Appl. Therm. Eng.*, vol. 123, pp. 1434–1443, Aug. 2017. DOI: [10.1016/j.applthermaleng.2017.05.198](https://doi.org/10.1016/j.applthermaleng.2017.05.198).
- [22] N. Tsuzuki, Y. Kato and T. Ishiduka, "High performance printed circuit heat exchanger," *Appl. Therm. Eng.*, vol. 27, no. 10, pp. 1702–1707, Jul. 2007. DOI: [10.1016/j.applthermaleng.2006.07.007](https://doi.org/10.1016/j.applthermaleng.2006.07.007).
- [23] N. Tsuzuki, Y. Kato, K. Nikitin and T. Ishiduka, "Advanced microchannel heat exchanger with S-shaped fins," *J. Nucl. Sci. Technol.*, vol. 46, no. 5, pp. 403–412, 2009. DOI: [10.1080/18811248.2007.9711547](https://doi.org/10.1080/18811248.2007.9711547).

- [24] X. Zhang, X. Sun, R. N. Christensen, M. Anderson and M. Carlson, "Optimization of S-shaped fin channels in a printed circuit heat exchanger for supercritical CO₂ test loop," presented at the 5th International Symposium-Supercritical CO₂ Power Cycles, San Antonio, Texas, March 29–31, 2016.
- [25] X. Xu, *et al.*, "Optimization of fin arrangement and channel configuration in an airfoil fin PCHE for supercritical CO₂ cycle," *Appl. Therm. Eng.*, vol. 70, no. 1, pp. 867–875, 2014. Sep DOI: [10.1016/j.applthermaleng.2014.05.040](https://doi.org/10.1016/j.applthermaleng.2014.05.040).
- [26] X. Y. Xu, Q. W. Wang, L. Li, S. V. Ekkad and T. Ma, "Thermal-hydraulic performance of different discontinuous fins used in a printed circuit heat exchanger for supercritical CO₂," *Numer. Heat. Tr. A-Appl.*, vol. 68, no. 10, pp. 1067–1086, 2015. DOI: [10.1080/10407782.2015.1032028](https://doi.org/10.1080/10407782.2015.1032028).
- [27] T. H. Kim, *et al.*, "Numerical analysis of air-foil shaped fin performance in printed circuit heat exchanger in a supercritical carbon dioxide power cycle," *Nucl. Eng. Des.*, vol. 288, pp. 110–118, Jul. 2015. DOI: [10.1016/j.nucengdes.2015.03.013](https://doi.org/10.1016/j.nucengdes.2015.03.013).
- [28] J. G. Kwon, T. H. Kim, H. S. Park, J. E. Cha and M. H. Kim, "Optimization of airfoil-type PCHE for the recuperator of small scale Brayton cycle by cost-based objective function," *Nucl. Eng. Des.*, vol. 298, pp. 192–200, Mar. 2016. DOI: [10.1016/j.nucengdes.2015.12.012](https://doi.org/10.1016/j.nucengdes.2015.12.012).
- [29] L. Chai and S. A. Tassou, "Modeling and evaluation of the thermohydraulic performance of compact recuperative heat exchangers in supercritical carbon dioxide waste heat to power conversion systems," *Heat Transfer Eng.*, vol. 43, no. 13, pp. 1067–1082, 2022. DOI: [10.1080/01457632.2021.1943833](https://doi.org/10.1080/01457632.2021.1943833).
- [30] W. Kim, Y.-J. Baik, S. Jeon, D. Jeon and C. Byon, "A mathematical correlation for predicting the thermal performance of cross, parallel, and counterflow PCHEs," *Int. J. Heat Mass Transfer*, vol. 106, pp. 1294–1302, Mar. 2017. DOI: [10.1016/j.ijheatmasstransfer.2016.10.110](https://doi.org/10.1016/j.ijheatmasstransfer.2016.10.110).
- [31] L. Chai and S. A. Tassou, "Numerical study of the thermohydraulic performance of printed circuit heat exchangers for supercritical CO₂ Brayton cycle application," *Energy Procedia*, vol. 161, pp. 480–488, Mar. 2019. DOI: [10.1016/j.egypro.2019.02.066](https://doi.org/10.1016/j.egypro.2019.02.066).
- [32] S. Mylavarapu, X. Sun, J. Figley, N. Needler and R. Christensen, "Investigation of high-temperature printed circuit heat exchangers for very high temperature reactors," *J. Eng. Gas. Turbine. Power*, vol. 131, no. 6, pp. 62905, Nov. 2009. DOI: [10.1115/1.3098425](https://doi.org/10.1115/1.3098425).
- [33] M. Chen, *et al.*, "Experimental and numerical study of a printed circuit heat exchanger," *Ann. Nucl. Energy*, vol. 97, pp. 221–231, Nov. 2016. DOI: [10.1016/j.anucene.2016.07.010](https://doi.org/10.1016/j.anucene.2016.07.010).
- [34] ANSYS fluent user's guide, release 19.0., Canonsburg, PA, 2018.
- [35] F. W. Dittus and L. M. K. Boelter, "Heat transfer in automobile radiators of the tubular type," *Univ. California Pub. Eng.*, vol. 2, no. 13, pp. 443–461, 1930.
- [36] V. Gnielinski, "New equations for heat and mass transfer in turbulent pipe and channel flow," *Int. Chem. Eng.*, vol. 16, no. 2, pp. 359–368, 1976.
- [37] P. R. H. Blasius, "The law on the compatibility of friction processes in liquid systems," *Forschungsheft*, vol. 131, no. 1, pp. 1–41, 1913.
- [38] B. S. Petukhov and P. L. Kirillov, "About heat transfer at turbulent fluid flow in tubes," *Therm. Eng.*, vol. 4, pp. 63–68, 1958.